

## Silicon Nanostructures for Photovoltaics

**Fabrice Gourbilleau,<sup>a</sup> Pratibha R. Nalini,<sup>b</sup> Julien Cardin,<sup>a</sup>  
Christian Dufour,<sup>a</sup> Odile Robbe,<sup>c</sup> Yannick Lambert,<sup>d</sup> Di Zhou,<sup>d</sup>  
Tao Xu,<sup>d</sup> and Didier Stiévenard<sup>d</sup>**

<sup>a</sup>*CIMAP/ENSICAEN, 6 Boulevard Maréchal Juin Caen, 14050 Cédex, France*

<sup>b</sup>*VIT Chennai, Vandalur-Kelambakkam Road, Chennai 600 127, Tamil Nadu, India*

<sup>c</sup>*PhLAM, UMR8523, Université de Lille 1, Villeneuve d'Ascq Cédex, France*

<sup>d</sup>*IEMN, UMR8520, Université de Lille 1, 59650 Villeneuve d'Ascq, Cédex, France*

fabrice.gourbilleau@ensicaen.fr

$\text{SiO}_x/\text{SiO}_2$  and  $\text{SiO}_x/\text{SiN}_x$  multilayers have been grown by reactive magnetron sputtering. Different fabrication parameters have been studied to optimize the density of Si nanoparticles (Si-nps) within the  $\text{SiO}_x$  sublayer. The aim is to favor the optical properties of the film as well as the carrier transport for the future development of Si-np-based solar device. This chapter evidences the beneficial role of the  $\text{SiN}_x$  sublayer on the achievement of good optical properties in a lower thermal budget with respect to the  $\text{SiO}_x/\text{SiO}_2$  counterparts. Moreover, the replacement of the  $\text{SiO}_2$  sublayer by the  $\text{SiN}_x$  one allows for a gain of two orders of magnitude of the conductivity of the film. These different multilayer structures have been deposited on the nanostructured substrate in a *p-i-n* configuration and photoconductance experiments have been carried out.

## 14.1 Introduction

Commercial single-junction crystalline and polycrystalline Si single-junction solar cells have dominated the photovoltaic (PV) market for years. But with the development of several new materials,<sup>1–10</sup> the increase in solar cell efficiency while keeping costs low has become a key issue for the Si solar industry. Among the different loss mechanisms limiting the efficiency of a single-junction solar cell,<sup>11</sup> the most important one is the relaxation of hot carriers<sup>12,13</sup> and the transmission of infrared photons. For the former, the excess energy provided by the absorption of energetic photons above the bandgap of the cell is lost by the thermalization of carriers. For the latter, the photons having energy below the bandgap of the cell are not absorbed by the cell and contribute to the losses. These loss mechanisms are primarily responsible of the theoretical efficiency limit of 30% for a single Si junction solar cell, as observed by Shockley and Queisser in 1961.<sup>14</sup> To overcome this spectral mismatch several solutions have been proposed to adapt either the solar spectrum to the absorption spectral range of the solar cell or the cell absorption spectral range to the solar spectrum. Adapting the solar spectrum consists in adding a layer, usually called photonic conversion layer, to the solar cell. Its role is either to transform one UV-visible photon energy to emit two IR photons<sup>15</sup> or to transform two sub-bandgap photons in one supra-bandgap photon.<sup>16</sup> In the both approaches the photons will be emitted by the conversion layer and, at the end, absorbed by the solar cell. The former process is called down-conversion (DC), while the latter is known as up-conversion (UC). Different approaches have been proposed in the literature to do the conversion: quantum cutting, up-conversion, down-shifting, and multi-exciton generation (MEG). Quantum cutting, to be efficient, requires the use of a couple of lanthanides ions such as Tb<sup>3+</sup>:Yb<sup>3+</sup>,<sup>17–19</sup> Ce<sup>3+</sup>:Yb<sup>3+</sup>,<sup>20,21</sup> and Pr<sup>3+</sup>:Yb<sup>3+</sup>.<sup>21–23</sup> For each of these systems the conversion efficiency is higher than 150%. More recently, our group succeeded in fabricating a DC layer compatible with the Si PV technology, for which a quantum efficiency as high as 183% has been evidenced.<sup>24</sup> The UC process currently observed in systems containing Er<sup>3+</sup> ions comprises at least two steps of excitation.<sup>25–27</sup> An internal

quantum yield of 12% has been achieved by Martín-Rodríguez et al.<sup>28</sup> The objective of the downshifting layer is to decrease the losses due to the thermalization process by converting one UV or blue photon to a yellow one. Different systems using lanthanides ions or nanoparticles have been reported.<sup>29–33</sup> These last authors<sup>33</sup> reported an increase in the external quantum efficiency of the solar cell from 15.3% to 15.46% by adding a Ce<sup>3+</sup>-doped yttrium garnet aluminum layer. The multiplication of the carriers or so-called MEG has been noticed for different quantum dots such as Si,<sup>34–36</sup> PbSe,<sup>36,37</sup> CdSe,<sup>38,39</sup> and so on. In these systems, the hot carriers created by the energetic photons of the solar spectrum give rise to the emission of two photons having a lower energy. Unfortunately, detrimental effects such as Auger recombination and/or intraband relaxation reduce drastically the efficiency of the process and consequently do not favor an increase in the solar cell yield. To enhance the absorption range of the solar spectrum, the cell structure has been adapted, giving rise to the tandem cell structure. This consists in stacking layers of different materials absorbing different parts of the solar spectrum. The use of amorphous silicon (a-Si) in a multi-junction solar cell/tandem cell has been the most popular choice over the years. Different junction devices with appropriately graded bandgaps can be placed in a stack to form a multi-junction device. The top junction absorbs the higher-energy photons and transmits the lower-energy photons to be absorbed by the bottom junctions. In the 1980s, remarkable advancements were made in the study of amorphous Si (a-Si)-based structures like silicon carbide, silicon nitride, etc. It has been demonstrated that the multi-junction tandem structures of a-Si such as a-SiC/a-Si heterojunctions as well as a-Si/poly-Si and a-Si/Ge alloys<sup>40</sup> could result in a stable multi-junction with reduced light-induced degradation<sup>41</sup> and improved efficiency. Another interesting approach is the used of hydrogenated microcrystalline silicon cells ( $\mu\text{c-Si}$ ), which are less sensitive to light-induced degradation than their crystalline counterparts.<sup>42</sup> More recently, the discovery of the quantum confinement (QC) effect<sup>43</sup> in porous silicon leading to an intense photoluminescence (PL) in the visible range at room temperature has attracted the interest of the photovoltaic community. This QC effect ascribed to the confinement of photogenerated

carriers in Si nanoparticles (size smaller than 8 nm)<sup>44,45</sup> allows the tuning of the Si bandgap through Si nanoparticle size. Thus a huge effort has been put into studies of Si nanoparticles embedded in an insulating matrix for PV application.<sup>46–48</sup> Thereby a first all-silicon tandem solar cell structure was achieved in 2008.<sup>49</sup> It appears that the controls of the Si grain size and density are key issues for monitoring the absorption properties, but also for allowing the transport of the carriers in the required insulating matrix for QC effect. Consequently the most appropriate way to achieve such a control is to fabricate multilayer structures formed by sandwiching a layer containing Si quantum dots between insulating layers playing the role of barrier.<sup>50</sup> The bandgap tuning ability associated with the increase of the light absorption efficiency in a compatible integrated Si technology process offers interesting perspectives for the third generation of solar cells, whose the aim is to decrease the cost of a cell below \$0.5/W.<sup>51</sup> Research on nanostructured Si-based structures for solar cell application is actually a promising field giving rise to a wide range of developments for which important disruptive results will probably be achieved in the next 10 years. Thus, the purpose of this chapter is to describe the fabrication and the optimization of the growth of Si quantum dots embedded in a silica matrix in two different multilayer structures: Si-rich silicon oxide (SiO<sub>x</sub>)/SiO<sub>2</sub> and Si-rich silicon oxide (SiO<sub>x</sub>)/Si-rich silicon nitride (SiN<sub>x</sub>). Microstructure and optical properties are investigated as a function of the fabrication conditions with the aim of achieving the best film structure having optimized optical and electrical properties required by an efficient solar device.

## 14.2 Experimental

SiO<sub>x</sub>/SiO<sub>2</sub> multilayers (MLs) are prepared by successively RF-sputtering a SiO<sub>2</sub> target alternatively in an Ar+H<sub>2</sub> reactive plasma to grow the Si-rich silicon oxide sublayer and in a pure Ar plasma to deposit the SiO<sub>2</sub> sublayer. Depending on the deposition parameters (hydrogen partial pressure, substrate temperature  $T_s$ , etc.), the reactive plasma allows the control of Si incorporation in the grown sublayer as already reported.<sup>52</sup>

During the deposition, the Si substrate is maintained at 500°C. MLs are annealed after deposition at different parameters (temperature and duration) in a N<sub>2</sub> flux. For the SiO<sub>x</sub>/SiN<sub>x</sub> MLs approach, the SiN<sub>x</sub> sublayer is achieved by either reactively sputtering a pure Si target in a nitrogen-rich plasma or co-sputtering a Si and Si<sub>3</sub>N<sub>4</sub> targets in a pure Ar plasma. In the first case the Si content is monitored by the N<sub>2</sub>/Ar partial pressure ratio, while in the second case it is controlled through the RF target power ratio applied on the targets ( $P_{\text{Si}}/(P_{\text{Si}} + P_{\text{Si}_3\text{N}_4})$ ). Different annealing conditions are applied to enhance the emission properties of the MLs and will be detailed hereafter. The microstructure of the deposited layers are investigated by means of several techniques, including (i) Fourier-transformed infrared spectroscopy (FTIR), (ii) X-ray diffraction (XRD), (iii) high-resolution transmission electron microscopy (HREM), and (iv) energy-filtered electron microscopy (EFTEM). The infrared absorption results allow the analysis of the Si-O and Si-N vibrations' bonds. The experiments were carried out using a Thermo Nicolet Nexus 670 spectrophotometer. XRD analyses were performed by means of Philips XPERT HPD Pro device with a CuK<sub>α</sub> radiation ( $\lambda = 0.1514$  nm) at a fixed grazing incidence of 0.5°. HREM and EFTEM experiments were made using a TEM-FEG microscope, Tecnai F20ST, equipped with an energy filter, TRIDIEM from Gatan. EFTEM images were obtained by inserting an energy-selecting slit in the energy dispersive plane of the filter at the Si ( $17 \pm 2$ ) eV and SiO<sub>2</sub> ( $23 \pm 2$ ) eV plasmon energies. The optical properties of the films were investigated by spectroscopic ellipsometry using a Jobin-Yvon ellipsometer (UVISEL) with an incident angle of 66.2°. The experimental spectra obtained have been fitted by a dispersion law based on the Forouhi-Bloomer model for amorphous semiconducting and insulating materials.<sup>53</sup> It allows the determination of the refractive index  $n$  and the absorption coefficient  $\alpha$  as a function of the photon energy. The emission properties of the fabricated multilayers were carried out by means of the 457 nm line of an Ar<sup>+</sup> laser (12.7 W cm<sup>-2</sup>) as an excitation source and a Hamamatsu photomultiplier after dispersion of the light in a Jobin-Yvon TRIAX-180 monochromator. The photoluminescence measurements (PL) were corrected from the spectral response of the setup.

## 14.3 SiO<sub>x</sub>/SiO<sub>2</sub> Multilayers

### 14.3.1 Reactive Magnetron Sputtering Approach

SiO<sub>x</sub>/SiO<sub>2</sub> multilayers are produced with the aim to favor the highest density of Si-Nps. The SiO<sub>x</sub> sublayers are deposited using a reactive plasma rich in hydrogen to sputter a pure SiO<sub>2</sub> target. Substrate temperature, the hydrogen partial pressure ( $P_{H_2}$ ), and RF power density applied on the SiO<sub>2</sub> target were the main deposition parameters, allowing control of the incorporation of the Si excess within the SiO<sub>x</sub> growing layer.<sup>54</sup> For this part, the hydrogen rate ( $r_H = P_{H_2}/(P_{H_2} + P_{Ar})$ ) was fixed at 80% to achieve the highest Si incorporation in the SiO<sub>x</sub> sublayer. To ensure a good phase separation and allow the formation of Si-nps, the films require a post-annealing treatment. Figure 14.1 shows the evolution of the two main vibrational modes LO<sub>3</sub> and TO<sub>3</sub> as a function of the annealing temperature ranging from 600°C to 1200°C in the case of a film annealed, constituted of a stack of 3 nm of SiO<sub>x</sub> and 3 nm

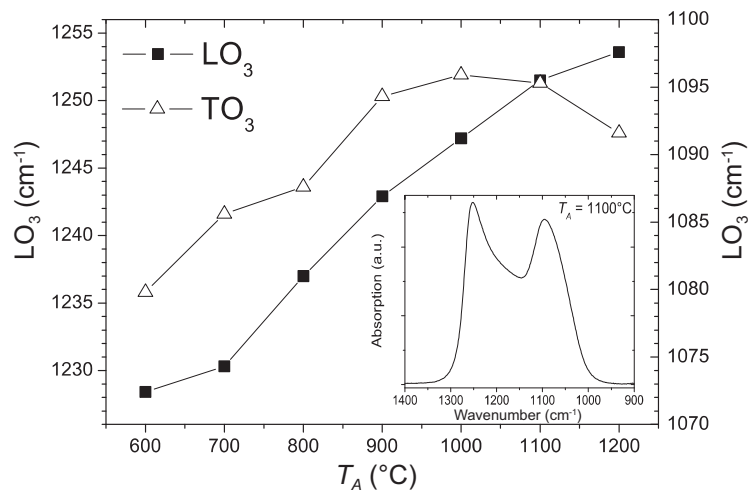


**Figure 14.1** Evolution of the maxima of LO<sub>3</sub> (left scale) and TO<sub>3</sub> (right scale) vibration modes for 3 nm SiO<sub>x</sub>/3 nm SiO<sub>2</sub> multilayers as a function of the annealing temperature,  $T_A$ . The annealing time was fixed at 1 hour. A typical registered FTIR spectrum is displayed in the inset for the films annealed at 1100°C.

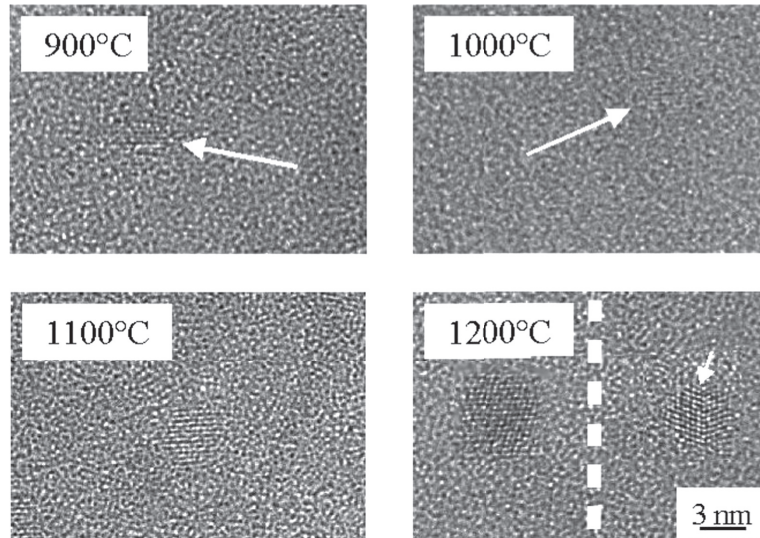


**Figure 14.2** HREM images of the 3 nm  $\text{SiO}_x$ /3 nm  $\text{SiO}_2$  multilayers for different annealing temperatures. The observations have been focused on the  $\text{SiO}_x$  sublayer to observe the formation of Si nanocrystals as evidenced by the arrow. For the highest annealing temperature some twinned grains have been noticed.

$\text{SiO}_2$  sublayers. As it is shown, the annealing process leads to a high energy shift of the  $\text{LO}_3$  and  $\text{TO}_3$  phonon peaks from 1125 to 1255  $\text{cm}^{-1}$  and from 1075 to 1095  $\text{cm}^{-1}$ , respectively. Such an evolution is correlated to a structural rearrangement in the  $\text{SiO}_2$  sublayer<sup>46</sup> and the phase separation occurring in the  $\text{SiO}_x$  one.<sup>55</sup>

The evolution of the microstructure can be seen on the HREM micrographies displayed in Fig. 14.2. These observations evidence the presence of Si nanocrystals after an annealing at 900°C for 1 hour. The diameter size (3 nm) is well controlled from 900°C to 1100°C, demonstrating the interest of such an ML structure. For the highest temperature, the thickness of the  $\text{SiO}_2$  barrier layer is not thick enough to avoid the diffusion of Si atoms, leading to an increase in Si-np size, which reaches here 5 nm.

The Si-np density is estimated through the combination of HREM-EFTEM observations in cross-sectional and plan-view configuration and reaches  $9 \times 10^{18}$  Nps  $\text{cm}^{-3}$ .<sup>47</sup> Such a value is

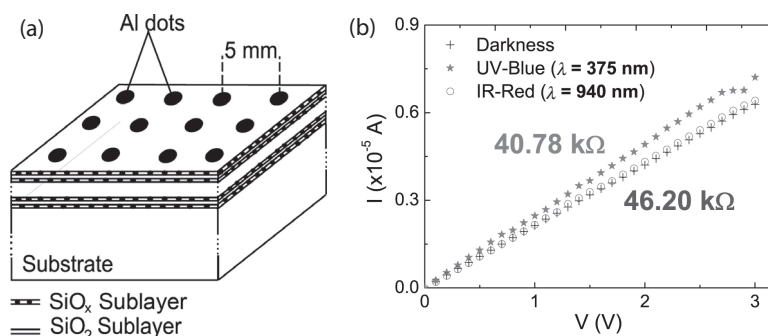


**Figure 14.3** (a) Scheme of the device of the  $I$ - $V$  measurements; (b)  $I$ - $V$  measurements under darkness, IR, and UV illuminations.<sup>46,47</sup>

achieved without percolation or coalescence between Si-nc, which is promising for the expected applications. Thus,  $I$ - $V$  measurements are carried out in the dark or under illumination. For this purpose a device constituted of 60 periods (3 nm SiO<sub>x</sub>/3 nm SiO<sub>2</sub>) is fabricated and annealed at 1100°C for 1 hour prior to the deposition of Al dots (1 mm diameter) separated from each other by 5 mm, as represented in Fig. 14.3a. Figure 14.3b presents the  $I$ - $V$  curves recorded under different illumination conditions.

The comparison between  $I$ - $V$  responses in the dark and under UV illumination evidences a photoconductance effect of the MLs deposited on the Si substrate with an increase in the conductivity. To confirm the role of the Si-nps in this enhancement,  $I$ - $V$  experiments are performed under infrared illumination—below the bandgap (Fig. 14.3b, cross). The recorded values are similar to those obtained in the dark, attesting the promising ML effect on photoconductance.

To optimize ML structures, several ways are tested and combined. The first consists in increasing the density of Si-nps to favor the conduction. The second aims at reducing the thermal budget considering that an annealing temperature as high as 1100°C for 1 hour is not possible for solar applications. At the end, the third one consists in favoring the carrier transport for which the use of a silica sublayer, even if the thickness is controlled, has a detrimental effect for this objective.

### 14.3.2 Reactive Magnetron Co-sputtering Approach

To achieve a higher Si excess in the  $\text{SiO}_x$  sublayer, a better way consists in coupling the reactive sputtering approach described above with a co-sputtering process. Thus, the fabrication of the  $\text{SiO}_x$  layer is achieved by simultaneously sputtering Si and  $\text{SiO}_2$  targets in a hydrogen-rich plasma. The use of hydrogen to incorporate Si excess in the growing  $\text{SiO}_2$  layer leads to a competition between deposition and etching according to the substrate temperature applied, as already reported in Ref. 54. Moreover, for a deposition temperature of  $500^\circ\text{C}$ , the presence of hydrogen favors the relaxation and the chemical annealing of the growing layer.<sup>56</sup> This is why the optimal hydrogen rate ( $r_{\text{H}}$ ) is chosen equal to 26%, considering that we will manage the incorporation of Si through the RF power density applied on the Si target ( $P_{\text{Si}}$ ). The one applied on the  $\text{SiO}_2$  target is fixed to  $7.4 \text{ W cm}^{-2}$ .

The effects of the  $P_{\text{Si}}$  on the optical property as well as the deposition rate are reported in Fig. 14.4. One can see that, as expected, the increase in  $P_{\text{Si}}$  favors the incorporation of Si within

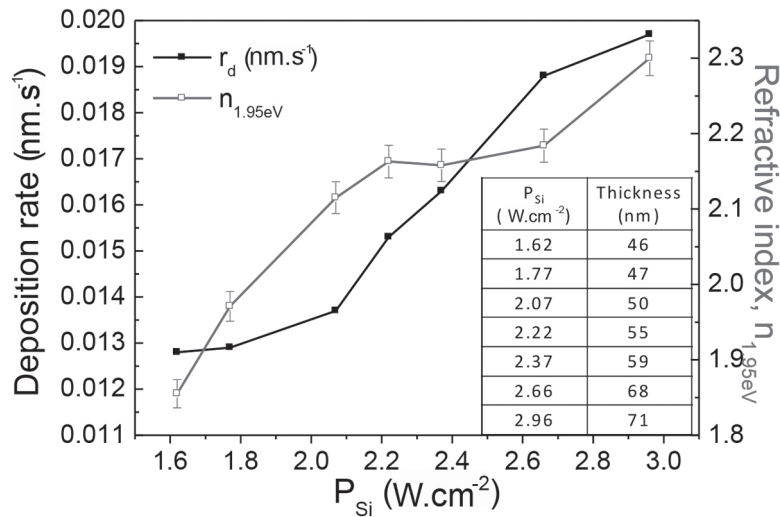


**Figure 14.4** Effect of the RF power density applied on the Si target ( $P_{\text{Si}}$ ) on the deposition rate (left axis), refractive index (right axis), and thickness (inset) of  $\text{SiO}_x$  layer deposited during 3600 s.

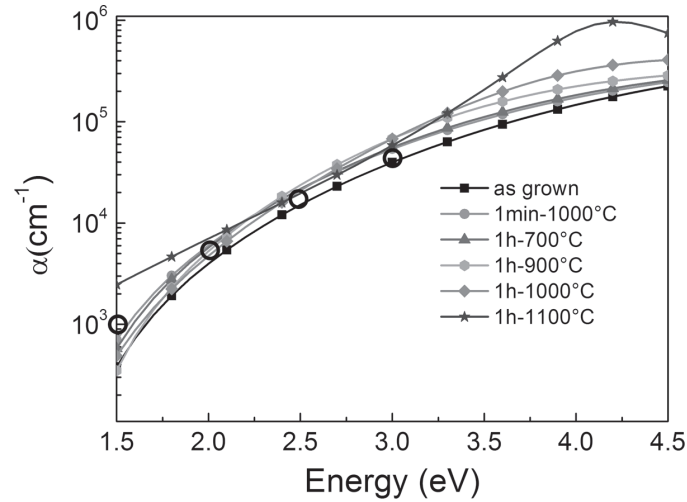


**Figure 14.5** Absorption coefficient for  $\text{SiO}_x$  thin films annealed at different temperatures. The hollow circles correspond to the  $\alpha_{\text{Si}}$  @ 1.5, 2, 2.5, and 3 eV.

the  $\text{SiO}_2$  matrix with a refractive index higher than 1.8. To allow the growth of a thin  $\text{SiO}_x$  sublayer in a reasonable time, the deposition rate is an important parameter. As for  $n$ ,  $P_{\text{Si}}$  leads to an increase in the deposition rate. Taking into account these two parameters, and keeping in mind that the aim of developing this reactive co-sputtering approach is to increase the Si-nc density but not to favor coalescence and/or percolation within the  $\text{SiO}_x$  sublayer in the multilayer structure, the intermediate  $P_{\text{Si}} = 2.22 \text{ W cm}^{-2}$  is chosen.

Figure 14.5 displays the absorption coefficient of the  $\text{SiO}_x$  thin film deposited with the deposition parameters fixed ( $T_s = 500^\circ\text{C}$ ,  $P_{\text{Si}} = 2.22 \text{ W cm}^{-2}$ ,  $r_{\text{H}} = 26\%$ ) and for different annealing treatments. The values of the absorption coefficient  $\alpha$  have been deduced from the ellipsometry measurements. They are reported in Fig. 14.5 in the 1.5–4.5 eV range. Whatever the annealing conditions,  $\alpha$  is of the order of  $10^4$ – $10^5 \text{ cm}^{-1}$ , showing a small increase with the annealing temperature. The maximum is reached after a treatment at  $1100^\circ\text{C}$  for 1 hour attributed to the crystallization of the Si excess, as evidenced in Fig. 14.6, by XRD experiments.  $\text{SiO}_x/\text{SiO}_2$  multilayers

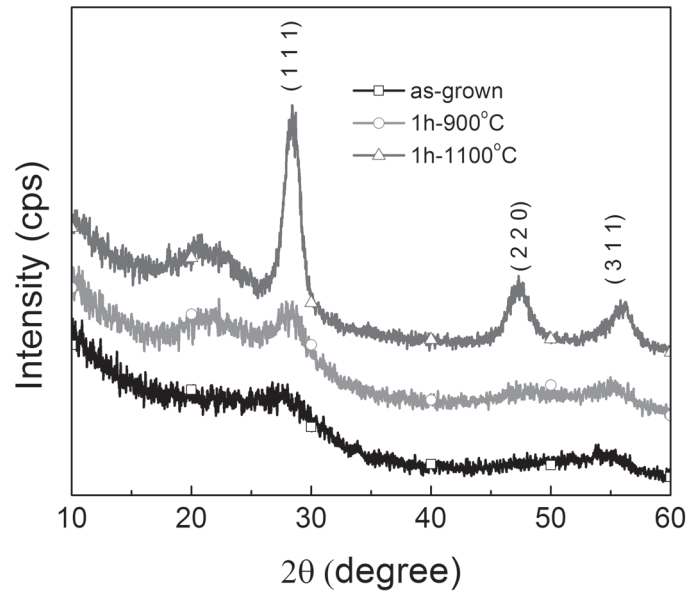


**Figure 14.6** X-ray diffraction spectra of  $\text{SiO}_x$  thin films.

are then fabricated and their microstructural and optical properties analyzed.

To evidence the quality of the multilayer we will here just present the photoluminescence spectrum achieved after an 1 hour annealing at  $1100^\circ\text{C}$  (Fig. 14.7). The emission evidenced by the PL measurements (488 nm excitation) attests the presence of Si-ncs within the  $\text{SiO}_x$  sublayer. The comparison with the  $\text{SiO}_x$  monolayer produced with the same deposition parameters demonstrated the interest in the multilayer approach, allowing control of the Si-nc size and distribution even in a high Si excess configuration. This Si excess is estimated by atom probe tomography (APT) (for more details on the technique see Ref. 57) and is about 18.5% within the  $\text{SiO}_x$  sublayer. The density of Si nanoparticles is estimated from the APT results and is found to be about  $3 \times 10^{19} \text{ np cm}^{-3}$ . As expected, by coupling the reactive approach and the co-sputtering process, we succeeded in achieving a higher density of Si nanoparticles with a controlled size.

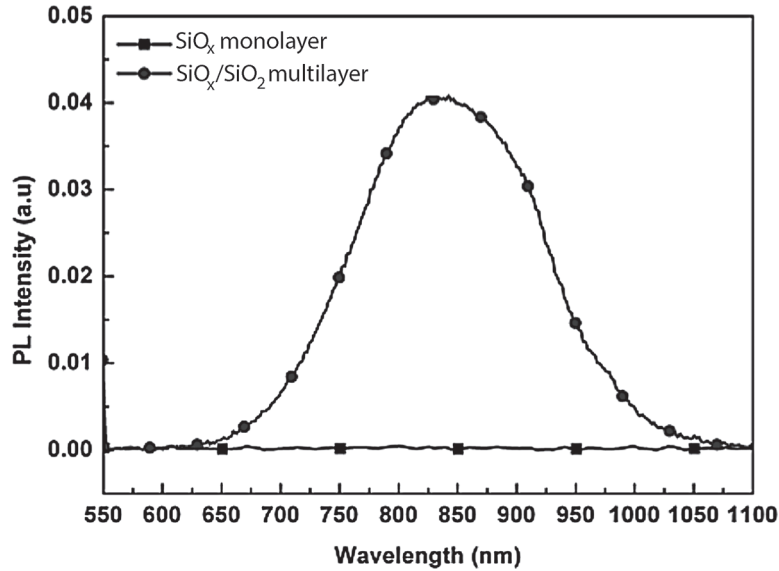


**Figure 14.7** Photoluminescence spectra of a 3 nm SiO<sub>x</sub>/3 nm SiO<sub>2</sub> multilayer and a SiO<sub>x</sub> layer. The deposition parameters for the SiO<sub>x</sub> layer and sublayer are the same for both films. The films have been annealed at 1100°C for 1 h.

The second (reducing the thermal budget) and third (favoring the carrier transport) points mentioned above to favor the development of Si nanostructure dedicated to solar cell applications will now be studied by replacing the SiO<sub>2</sub> insulating barrier by a lower-bandgap material: SiN<sub>x</sub>.

## 14.4 SiO<sub>x</sub>/SiN<sub>x</sub> Multilayers

### 14.4.1 SiN<sub>x</sub> Layer, a Reactive Magnetron Sputtering Approach

It has been recently demonstrated that whatever the deposition approach used, the SiN<sub>x</sub> optical properties are linked to the value of the refractive index.<sup>58</sup> This is why SiN<sub>x</sub> layers were grown by sputtering a Si cathode in a nitrogen-rich Ar plasma. The RF power density applied on the Si target was fixed at 4.44 W cm<sup>-2</sup> and the

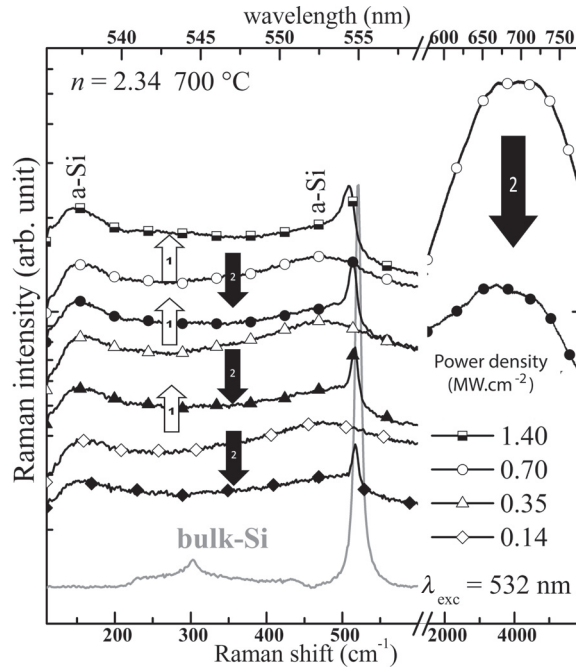


**Figure 14.8** Raman spectra of a  $\text{SiN}_x$  film for different Raman laser power densities. The  $\text{SiN}_x$  film is deposited on fused silica substrates.

plasma pressure to 3 mTorr. The composition of the nitride film was analyzed through the variation of the nitrogen rate  $r_N$ , which corresponds to the ratio of the nitrogen partial pressure to the total pressure. By varying the  $r_N$  value from 5 to 16%, the refractive index at 1.95 eV of the layer was found to be in the 1.9–3.3 range.

The microstructure of the  $\text{SiN}_x$  films was investigated using Raman spectroscopy to analyze the formation of Si-nps. Figure 14.8 shows Raman spectra recorded on a  $\text{SiN}_x$  layer having a refractive index of 2.34. One can observe in this figure that the increase (white arrow and empty symbols) in the Raman laser power density from 0.14 to 0.70  $\text{MW cm}^{-2}$  does not modify the microstructure of the layer whereas an intense PL emission is noticed. When the excitation power density reaches 1.4  $\text{MW cm}^{-2}$  a sharp Raman peak appears that is slightly shifted from that of bulk c-Si, which proves the formation of Si-nps in the  $\text{SiN}_x$  film. When the Raman laser

power density is decreased (black arrows and full symbols), this Raman peak remains, attesting that the layer has been definitively modified under a laser annealing process. Such a formation of Si-nps under laser has been already observed elsewhere.<sup>59,60</sup> The formation of these Si-nps has led to the quenching of the PL, as shown in the figure. Moreover, a deep study<sup>58</sup> performed on the optical properties of SiN<sub>x</sub> films depending on the refractive index value and the annealing temperature has proved that for  $n \leq 2.4$  the layers exhibit the highest PL intensity after annealing at 900°C for 1 hour.<sup>58</sup> When higher Si excess is incorporated, i.e.,  $n > 2.4$ , no PL is observed, whatever the annealing temperature applied.<sup>58</sup> Considering these results, the nitride sublayer in the ML approach is grown with an achieved Si excess of 11 at.% (determined by RBS experiments).

#### 14.4.2 SiO<sub>x</sub>/SiN<sub>x</sub> Multilayers

SiO<sub>x</sub>/SiN<sub>x</sub> multilayers are grown by successive deposition of SiO<sub>x</sub> and SiN<sub>x</sub> sublayers on a 2" Si wafer using the optimized conditions described above. The thickness of the SiO<sub>x</sub> sublayer is fixed to 3.5 nm, while that of the SiN<sub>x</sub> one is fixed to 5 nm. The MLs are constituted of 50 periods of this SiO<sub>x</sub>/SiN<sub>x</sub> pattern. The substrate temperature is maintained at 500°C during the deposition process. After deposition the MLs are annealed by means of either conventional or rapid thermal annealing approaches.

Emission properties of these MLs structures are studied by means of Ar<sup>+</sup> 488 nm continuous laser excitation for different annealing temperatures (Fig. 14.9). First of all, one can notice that the best annealing treatment usually applied to SiO<sub>x</sub>/SiO<sub>2</sub> MLs<sup>46</sup> leads to the total quenching of the photoluminescence of the SiO<sub>x</sub>/SiN<sub>x</sub> MLs. For long-time annealing treatments the nitride ML requires lower temperatures (400–700°C) to exhibit significant emission. The maximum emission intensity is obtained at 1000°C but for only 1 min treatment, and this intensity is more than two times higher than that of SiO<sub>x</sub>/SiO<sub>2</sub> 1100°C 1 h. Note that for such a short treatment, SiO<sub>x</sub>/SiO<sub>2</sub> MLs do not show any emission.

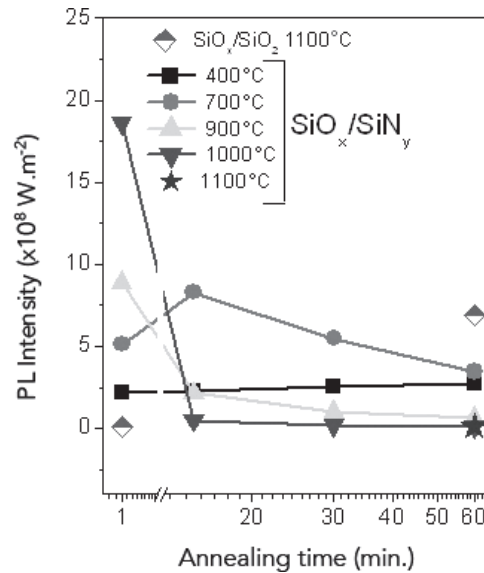


**Figure 14.9** Maximum PL intensity evolution of 3.5 nm SiO<sub>x</sub>/5 nm SiN<sub>x</sub> MLs as a function of the annealing time for different annealing temperatures. The emission of the equivalent SiO<sub>x</sub>/SiO<sub>2</sub> ML annealed at 1100°C for 1 h is reported for comparison.

The microstructure of strongest photoluminescent MLs has been studied by HREM and EFTEM (Fig. 14.10). These observations evidence the presence of Si nanoparticles having an average diameter of about 3.4 nm. The EFTEM image achieved by filtering the energy at the Si plasmon (17 eV) confirms the high density of Si-nps ( $\sim 10^{19}$  np cm<sup>-3</sup>) noticed in SiO<sub>x</sub>/SiO<sub>2</sub> MLs by atom probe tomography, but here it has been achieved at a lower temperature and shorter time than in the case of SiO<sub>x</sub>/SiO<sub>2</sub> MLs (1100°C – 1h). These Si-nps are only localized within the SiO<sub>x</sub> sublayer. No trace of Si-nps has been observed within the SiN<sub>x</sub> sublayers. This result can be explained by an insufficient Si incorporation and/or a too low annealing temperature along with a too short annealing time for the formation and growth of Si seeds in a thin SiN<sub>x</sub> sublayer. The filtering at the SiO<sub>2</sub> plasmon peak (27 eV) shows that there is no oxide formation within the SiN<sub>x</sub> sublayer. These observations attest that

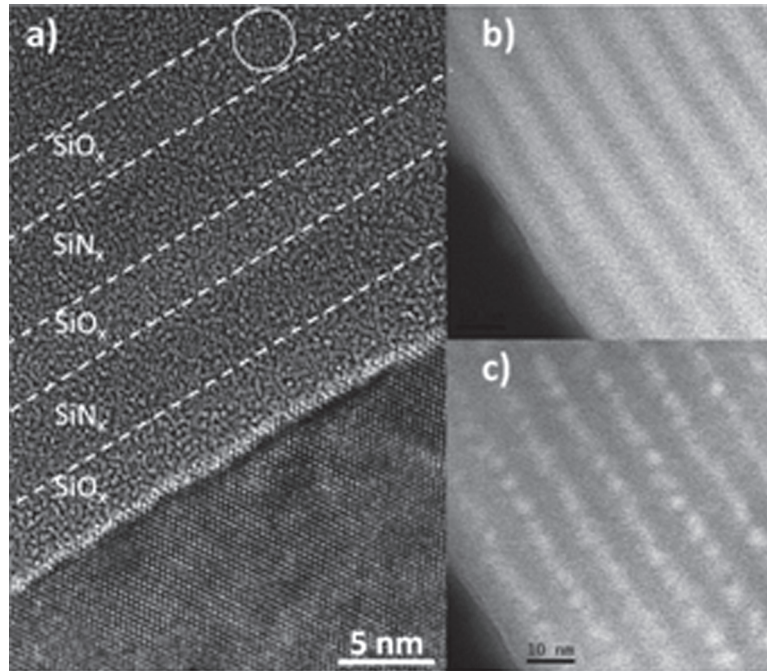


**Figure 14.10** (a) HREM image of 3.5 nm SiO<sub>x</sub>/5 nm SiN<sub>x</sub> MLs; (b, c) EFTEM images by filtering the energy at SiO<sub>2</sub> plasmon (23 eV), and Si plasmon (17 eV), respectively. The film has been annealed at 1000°C for 1 min.

the PL emission presented in Fig. 14.9 is coming from the presence of Si-nps. The electrical properties are carried out on a 850 nm thick SiO<sub>x</sub>/SiN<sub>x</sub> ML annealed at 1000°C for 1 minute. The results have been reported in Fig. 14.11 with the ones achieved on a 140 nm thick SiO<sub>x</sub>/SiO<sub>2</sub> ML. At 7.5 eV, the deduced resistivity decreases from 214 MΩ to 2.15 MΩ. It is a promising result demonstrating the interest of replacing the SiO<sub>2</sub> sublayer by a SiN<sub>x</sub> one in order to enhance the carrier transport.

These results evidence the advantages of using the new SiO<sub>x</sub>/SiN<sub>x</sub> multilayer structure in the fabrication of films for future solar application. In what follows, we compare the optical and electrical properties of these MLs on a nanostructured substrate.

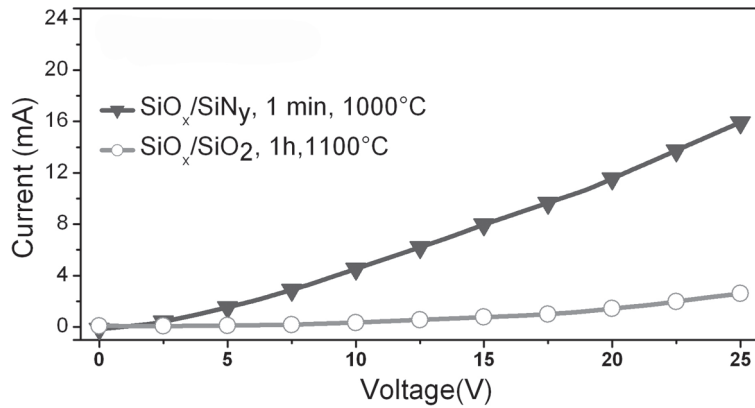


**Figure 14.11** Comparison of the  $I$ - $V$  behavior between 3.5 nm  $\text{SiO}_x$ /5 nm  $\text{SiN}_x$  and 3.5 nm  $\text{SiO}_x$ /3.5 nm  $\text{SiO}_2$  MLs annealed in the optimized conditions for achieving PL emission.

## 14.5 Nanostructured Substrate

### 14.5.1 Nanocone Fabrication

To fabricate the nanocones (NCs), low-cost masks with suitable sizes were deposited on the substrate. We choose silica balls (Gmbh Microparticles Company) to form the mask and the Langmuir-Blodgett (LB) technique to deposit modified silica monolayer on the Si substrate. The initial diameter of the silica balls gives the periodicity of the NCs. To satisfy the needs of the LB technique and obtain amphiphilic silica balls, surface modification is required. The steps of the experimental process are as follows:

- (1) 1 mL of silica ball solution (5% in water) is centrifuged at 5000 tr/min for 4 minutes. Then, the supernatant is removed and replaced by 1.5 mL of ethanol. This new solution is put in the ultrasonic bath to be well dispersed and then is centrifuged again to remove the supernatant and replaced by ethanol.
- (2) 10  $\mu\text{L}$  of aminopropyl-dimethyl-ethoxy silane is put into the solution to react with particles for 24 hours at room temperature.

- (3) Centrifugal and ultrasonic processes, similar to step (1), are repeated three times. The modified silica balls are diluted into the mixture of 250  $\mu\text{L}$  ethanol and 250  $\mu\text{L}$  chloroform. Thanks to the amphiphilic nature of modified silica balls, when silica balls spread at the air/water interface, the hydrophilic group is immersed in the water and the hydrophobic part points towards the air. The monolayer can be compressed by the barrier-moving system. Meanwhile, the surface pressure is measured by electrobalance.

Silica balls can be transferred into the substrate by successively dipping the substrate down and up through the monolayer under a constant surface pressure (pressure of dip-coating). Any contamination will lower surface tension, so the cleaning steps are performed before the deposition process: chloroform, isopropanol, and deionized water are used successively to wash the LB trough.

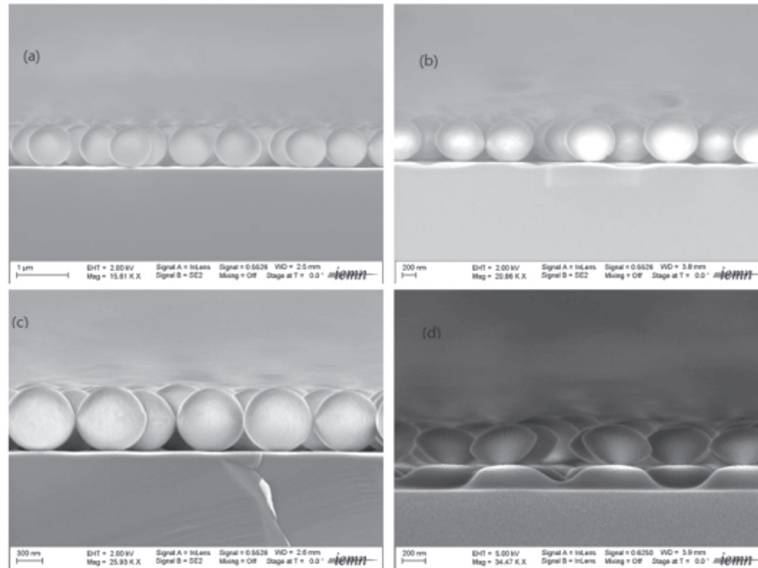
In order to obtain NCs with required top or bottom diameters, silica balls are reduced by RIE plasma etching system. We use  $\text{CHF}_3$  and  $\text{O}_2$  to etch silica balls. The parameters of the plasma are given in Table 14.1.

Figure 14.12 shows the morphology of reduced silica balls with different parameters. The variation of power and pressure results in the configuration change of silica balls. When silica balls have been reduced to a required size, RIE technique is used to fabricate NCs.

Figure 14.13 is an illustration of the morphology of nanocones obtained by RIE etching ( $\text{CHF}_3$  [40 sccm],  $\text{O}_2$  [8 sccm], power [100 W] and a pressure of 250 mTorr). Finally, after etching, we remove the remaining silica balls by immersing them into HF solution (50% HF) for 30 seconds. In the following, the dimensions of the nanocones are 700 nm at the bottom, 165 nm at the top, 440 nm for the

**Table 14.1** RIE parameter for etching silica balls

|   | $\text{CHF}_3$ (sccm) | $\text{O}_2$ (sccm) | Power (W) | Pressure (mTorr) |
|---|-----------------------|---------------------|-----------|------------------|
| a | 40                    | 8                   | 50        | 300              |
| b | 40                    | 8                   | 70        | 350              |
| c | 40                    | 8                   | 100       | 550              |
| d | 40                    | 8                   | 100       | 250              |



**Figure 14.12** SEM images of reduced silica balls with different etching parameters, images (a), (b), (c), and (d) correspond to parameters a, b, c, d in Table 14.1, respectively.

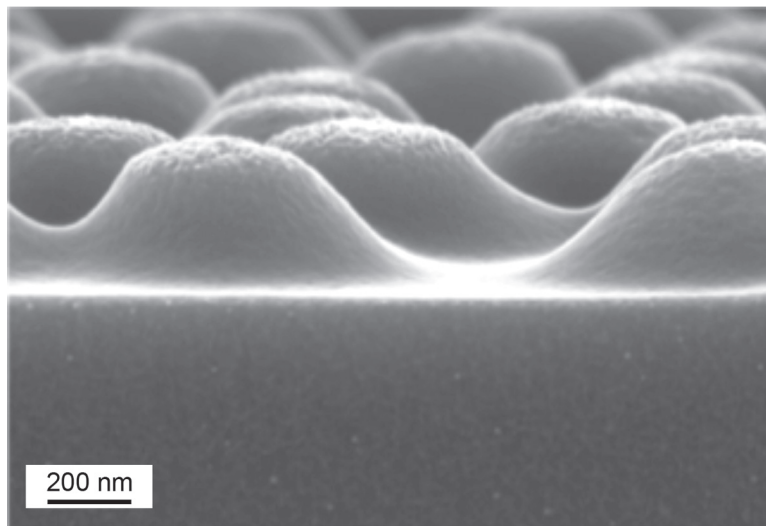


**Figure 14.13** SEM images of Si nanocones made by RIE etching.

height, and with an average density of  $1.5 \times 10^8$  nanocones  $\text{cm}^{-2}$ . Together with  $I$ - $V$  curves, photoconductivity measurements are performed using a monochromated source (ORIEL), with a 150 W Xenon light, allowing a spectroscopic analysis from 300 nm to 1100 nm. The photon flux is calibrated using a thermopile detector with a broad flat spectral response from 200 nm to 50  $\mu\text{m}$ . All the photocurrent curves are, therefore, normalized. In order to increase the signal/noise ratio, the light flux is chopped at a frequency of 30 Hz and a lock-in detection.<sup>61</sup>

### 14.5.2 *Films on Nanostructured Substrate*

Different layers are deposited on the nanostructured substrates. They consist of (i) a 4 nm thick  $\text{SiO}_x$  layer (sample 1458), (ii) 10 patterns of 4 nm  $\text{SiO}_x$ /1.5 nm  $\text{SiO}_2$  (sample 1459), (iii) one pattern of 4 nm  $\text{SiO}_x$ /1.5 nm  $\text{SiN}_x$  (sample 1461). In order to check the morphology of the layers, SEM analysis are performed, as illustrated in Fig. 14.14, and are confirmed by TEM observations in the cross-section sample (not shown here). Figure 14.14a shows a view of the nanocones covered with the polysilicon layers. The use of nanocones allows a good conformal polysilicon layer on the surface of the NCs, which is very difficult to achieve with nanowires. Figure 14.14b is obtained on a cleaved sample and the oxide layer is clearly observed (black contrast), with an average thickness of 46 nm, in agreement with the stack of 10 periods of 4 nm  $\text{SiO}_x$ /1.5 nm  $\text{SiO}_2$  (sample 1459).

### 14.5.3 *Electrical Properties*

In order to correlate the thickness of the oxide layers with their electrical properties,  $n$ - $p$  junctions were fabricated. Their structure is described hereafter: 80 nm thick of a  $n^+$  polysilicon layer is deposited on the top of a 100-nm thick intrinsic  $i$  layer. The latter is deposited on the insulating sputtered film containing Si-nps (4 to 45 nm thick). These stacked layers are fabricated on a  $p$ -doped substrate with a typical space charge region of 40 nm, deduced from its doping level. We perform current-voltage ( $I$ - $V$ ) measurements, at room temperature, as illustrated in Fig. 14.15. From these curves,

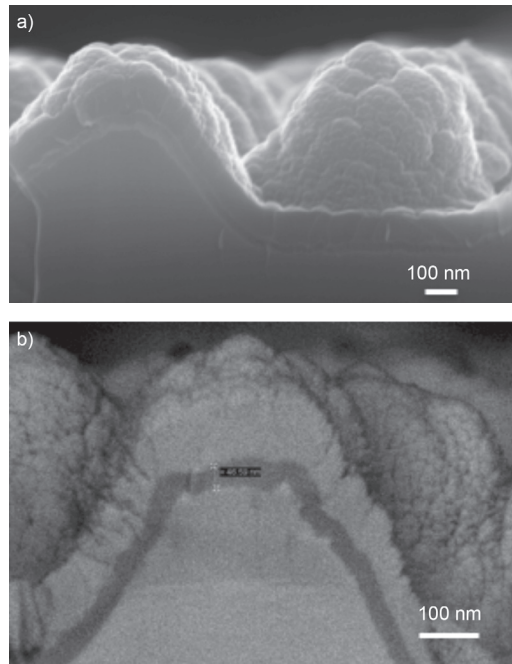


**Figure 14.14** SEM images of the 1459 sample (10 patterns of 4 nm  $\text{SiO}_x$ /1.5 nm  $\text{SiO}_2$ ).

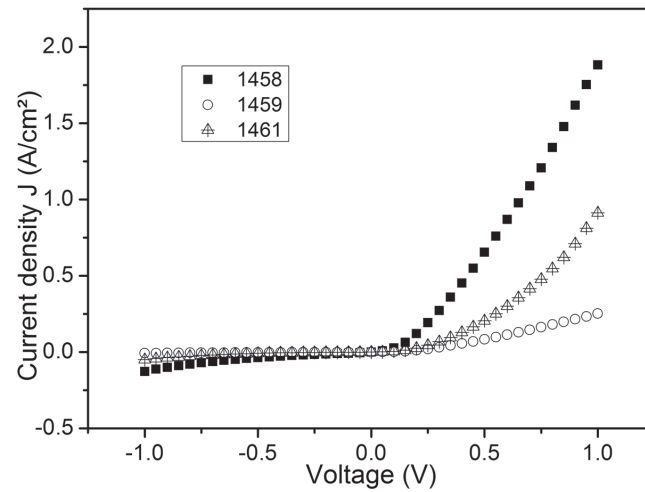


**Figure 14.15**  $I$ - $V$  curves of the three samples (1458, 1459, and 1461).

**Table 14.2** Comparison of the electrical properties for different insulating thicknesses

| Samples  | Total of insulating thickness (nm) | Serial resistance ( $\Omega$ ) | Ratio of resistances          | Ratio of the insulating thicknesses |
|--|------------------------------------|--------------------------------|-------------------------------|-------------------------------------|
| <b>1458</b><br>1 period 4 nm<br>$\text{SiO}_x$ annealed<br>30 min 1100°C                           | 4                                  | 38                             | $1461/1458$<br>$52/38=1.37$   | $1461/1458$<br>$5.5/4 = 1.37$       |
| <b>1459</b><br>10 period 4 nm<br>$\text{SiO}_x/1.5$ nm $\text{SiO}_2$<br>annealed 30 min<br>1100°C | 45                                 | 270                            | $1459/1458$<br>$270/38 = 7.1$ | $1459/1458$<br>$45/5.5 = 11.25$     |
| <b>1461</b><br>1 period 4 nm<br>$\text{SiO}_x/1.5$ nm- $\text{SiN}_x$<br>annealed 1 min<br>1000°C  | 5.5                                | 52                             |                               |                                     |

we deduce electrical properties summarized in the Table 14.2 considering that the films are constituted of an insulating matrix.

From the comparison of the serial resistance (directly bound to the oxide layer and measured as the average slope of the  $I-V$  curves between 0.25 and 1 V) and the oxide thicknesses of the sample 1461 and 1458, we find the same ratio between the oxide thicknesses and the resistances. This means that the insulating resistance is proportional to the thickness, i.e., the layers are homogeneous and the resistance of the  $\text{SiO}_x$  or  $\text{SiN}_x$  are equivalent. A priori, the thermal annealing used for sample 1461 is efficient, whereas its temperature is lower and its duration is only 1 min compared to 30 min. Second, if we compare samples 1459 and 1458, we find that the ratio obtained for the serial resistance is lower than the one obtained for the thickness: for a higher number of sublayers, there is an improvement in the resistivity after the thermal annealing.

To correlate these observations with optical properties, photoconductivity measurements have been performed and summarized in Fig. 14.16. First, we measure a lower photocurrent in nanostructured structures compared to planar junctions even if these nanostructured structures exhibit a better optical absorption. This

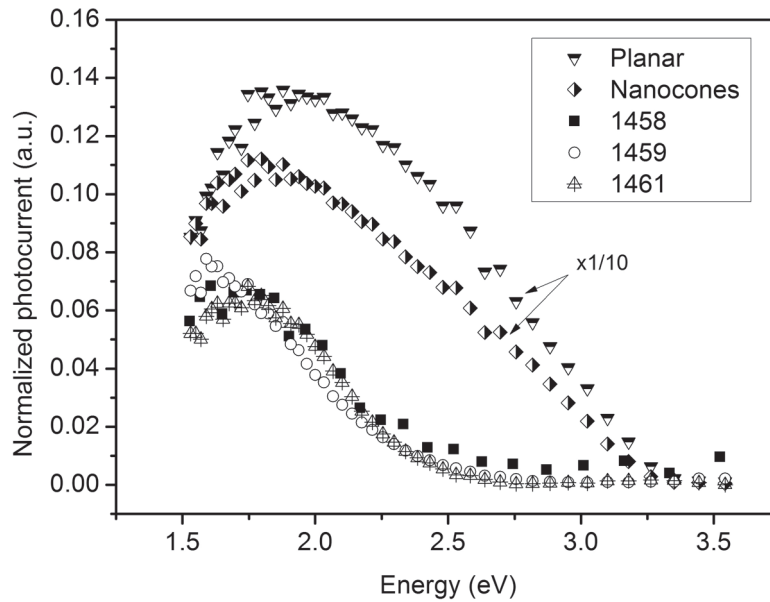


**Figure 14.16** Comparison of photoconductivity measurements between planar, nanostructured, and nanostructured plus  $\text{SiO}_x$  (1458),  $\text{SiO}_x/\text{SiO}_2$  (1459), and  $\text{SiO}_x/\text{SiN}_x$  (1460) layers.

is due to the effect of the surface increase associated with the nanocone structure.<sup>62</sup> Consequently, one can expect higher surface defects responsible for the achievement of this lower photocurrent (Fig. 14.16). Efficient passivation is necessary to recover these surface defects and get a better photocurrent (not treated in this work).

As regards the nanostructured samples, sample 1459 exhibits the lowest current, typically a factor of 2 less than the photocurrent detected in samples 1458 and 1461. These two samples exhibit the same photocurrent, with an amplitude lower by a factor of 10 compared to the nanostructured sample. So, we observe that the detected photocurrent, in the presence of oxide layers, is lower than the photocurrent detected in samples without oxide layers. These first observations show that these layers, made of silicon nanocrystallites embedded in oxide layers, are inefficient in producing photocurrent through conversion mechanism.

Such a decrease in the photocurrent can be explained considering the absorption of photons in the oxide layers. In this case, without any conversion efficiency, i.e., without the creation of photocurrent in the registered energy range, one can only observe a decrease in the photocurrent. In fact, as illustrated in Fig. 14.5, in the range 1.5–3 eV, the absorption coefficients ( $\alpha$ ) of silicon (hollow circle) and of the  $\text{SiO}_x$  layer that contains the Si-nps have the same amplitude. So, it is straightforward to estimate the relative absorption of photons in the oxide layer with respect to the absorption of photons in the silicon layers, in which the presence of an electric field allows the separation of the photocarriers. The total silicon thickness where the electric field is non-zero is the sum of the  $n^+$ ,  $i$ , and  $p$ -depleted layers, i.e.,  $80 + 100 + 40 = 220$  nm, to be compared to the 4 to 45 nm thickness of the oxide layers. As the absorption is proportional to  $\exp(-\alpha d)$  where  $d$  is a thickness, the absorbed photons in the oxide layers is less than 3 % (for 5 nm thick) or 25% (45 nm thick) with respect to the ones absorbed in the silicon layers (taking  $d$  equal to 220 nm). So, the absorption in the oxide layers, without the creation of photocurrent, cannot explain the decrease by a factor of 10 of the photocurrent.

Consequently, we propose that these layers introduce a barrier of a few electron-volts inside the structure so that the excitons created in the silicon layers are blocked by this barrier and therefore recombine. This effect is amplified by the fact that we use polysilicon  $n^+$  and  $i$  layers, known to have a great density of recombination centers.

## 14.6 Conclusions

This chapter aims at investigating different approaches to improve the optical and electrical properties of Si-np-rich films for future solar cell application. It demonstrates the interest in working with a controlled Si-np size through a multilayer approach. To overcome the insulating properties of the silica sublayer, a new structure has been developed and the results achieved are promising for future developments in photovoltaics. This new structure, consisting of the stacking of  $\text{SiO}_x$  and  $\text{SiN}_x$  sublayers with a controlled thickness,

presents better optical and electrical properties than its  $\text{SiO}_x/\text{SiO}_2$  counterparts. Moreover, it allows to reduce the thermal budget, moving from a treatment at  $1100^\circ\text{C}$  for 1 hour (for  $\text{SiO}_x/\text{SiO}_2$  MLs) to  $1000^\circ\text{C}$  for 1 min ( $\text{SiO}_x/\text{SiN}_x$  MLs). Optimization of the annealing treatment as well as the thickness and the Si excess of the  $\text{SiN}_x$  sublayer are the steps that improve the optical and electrical properties. As shown by the photoconductance measurements, these optimizations coupled with an adapted annealing process to recover the defects are promising for developing new efficient absorbers for the next generation of solar cells.

## Acknowledgments

This study has been partially supported by the *Labex EMC3* through the research program ASAP and by the French Research National Agency through the project GENESE (No. ANR-13-BS09-0020-01). The authors thank Xavier Portier from CIMAP for HREM observations and Marzia Carrada from CEMES-Toulouse for HREM and EFTEM observations.

## References

1. M. D. Kelzenberg, D. B. Turner-Evans, M. C. Putnam, S. W. Boettcher, R. M. Briggs, J. Y. Baek, N. S. Lewis, and H. A. Atwater, *Energy Environ. Sci.* **4**, 866 (2011).
2. S. Jeong, M. D. McGehee, and Y. Cui, *Nat. Commun.* **4**, 2950 (2013).
3. A. T. Barrows, A. J. Pearson, C. K. Kwak, A. D. F. Dunbar, A. R. Buckley, and D. G. Lidzey, *Energy Environ. Sci.* **7**, 2944 (2014).
4. B. A. MacLeod, P. Schulz, S. R. Cowan, A. Garcia, D. S. Ginley, A. Kahn, and D. C. Olson, *Adv. Energy Mater.* **4**, 1400073 (2014).
5. G. Hodes and D. Cahen, *Nat. Photon.* **8**, 87 (2014).
6. D. Liu and T. L. Kelly, *Nat. Photon.* **8**, 133 (2014).
7. M. G. Panthani, J. M. Kurley, R. W. Crisp, T. C. Dietz, T. Ezzyat, J. M. Luther, and D. V. Talapin, *Nano Lett.* **14**, 670 (2014).
8. S. Mathew, A. Yella, P. Gao, R. Humphry-Baker, B. F. E. Curchod, N. Ashari-Astani, I. Tavernelli, U. Rothlisberger, M. K. Nazeeruddin, and M. Grätzel, *Nat. Chem.* **6**, 242 (2014).

9. J. J. Intemann, K. Yao, Y.-X. Li, H.-L. Yip, Y.-X. Xu, P.-W. Liang, C.-C. Chueh, F.-Z. Ding, X. Yang, X. Li, Y. Chen, and A. K.-Y. Jen, *Adv. Funct. Mater.* **24**, 1465 (2014).
10. W. Wang, M. T. Winkler, O. Gunawan, T. Gokmen, T. K. Todorov, Y. Zhu, and D. B. Mitzi, *Adv. Energy Mater.* **4**, 1301465 (2014).
11. B. S. Richards, *Sol. Energy Mater. Sol. Cells* **90**, 2329 (2006).
12. B. M. van der Ende, L. Aarts, and A. Meijerink, *Phys. Chem. Chem. Phys.* **11**, 11081 (2009).
13. S. Saeed, E. M. L. D. de Jong, K. Dohnalova, and T. Gregorkiewicz, *Nat. Commun.* **5**, 4665 (2014).
14. W. Shockley and H. J. Queisser, *J. Appl. Phys.* **32**, 510 (1961).
15. T. Trupke, M. A. Green, and P. Würfel, *J. Appl. Phys.* **92**, 1668 (2002).
16. C. Strümpel, M. McCann, G. Beaucarne, V. Arkhipov, A. Slaoui, V. Švrček, C. del Cañizo, and I. Tobias, *Sol. Energy Mater. Sol. Cells* **91**, 238 (2007).
17. P. Vergeer, T. J. H. Vlugt, M. H. F. Kox, M. I. den Hertog, J. P. J. M. van der Eerden, and A. Meijerink, *Phys. Rev. B* **71**, 014119 (2005).
18. Q. Y. Zhang, G. F. Yang, and Z. H. Jiang, *Appl. Phys. Lett.* **91**, 051903 (2007).
19. M. Kochanowicz, D. Dorosz, J. Zmojda, J. Dorosz, J. Pisarska, and W. A. Pisarski, *Opt. Mater. Express* **4**, 1050 (2014).
20. D. Chen, Y. Wang, Y. Yu, P. Huang, and F. Weng, *J. Appl. Phys.* **104**, 116105 (2008).
21. E. van der Kolk, O. M. Ten Kate, J. W. Wiegman, D. Biner, and K. W. Krämer, *Opt. Mater.* **33**, 1024 (2011).
22. D. Serrano, A. Braud, J.-L. Doualan, P. Camy, and R. Moncorgé, *J. Opt. Soc. Am. B* **28**, 1760 (2011).
23. A. Guille, A. Pereira, and B. Moine, *APL Mater.* **1**, 062106 (2013).
24. Y.-T. An, C. Labbé, J. Cardin, M. Morales, and F. Gourbilleau, *Adv. Opt. Mater.* **1**, 855 (2013).
25. C. M. Johnson, S. Woo, and G. J. Conibeer, *IEEE J. Photovolt.* **4**, 799 (2014).
26. S. K. W. MacDougall, A. Ivaturi, J. Marques-Hueso, K. W. Krämer, and B. S. Richards, *Sol. Energy Mater. Sol. Cells* **128**, 18 (2014).
27. M. Rüdiger, S. Fischer, J. Frank, A. Ivaturi, B. S. Richards, K. W. Krämer, M. Hermle, and J. C. Goldschmidt, *Sol. Energy Mater. Sol. Cells* **128**, 57 (2014).
28. R. Martín-Rodríguez, S. Fischer, A. Ivaturi, B. Froehlich, K. W. Krämer, J. C. Goldschmidt, B. S. Richards, and A. Meijerink, *Chem. Mater.* **25**, 1912 (2013).

29. J.-Y. Chen, C. K. Huang, W. B. Hung, K. W. Sun, and T. M. Chen, *Sol. Energy Mater. Sol. Cells* **120**, 168 (2014).
30. S. Kalytchuk, S. Gupta, O. Zhovtiuk, A. Vaneski, S. V. Kershaw, H. Fu, Z. Fan, E. C. H. Kwok, C.-F. Wang, W. Y. Teoh, and A. L. Rogach, *J. Phys. Chem. C* **118**, 16393 (2014).
31. A. Apostoluk, Y. Zhu, B. Masenelli, J.-J. Delaunay, M. Sibiński, K. Znajdek, A. Focsa, and I. Kaliszewska, *Microelectron. Eng.* **127**, 51 (2014).
32. F. Sgrignuoli, P. Ingenhoven, G. Pucker, V. D. Mihailetchi, E. Froner, Y. Jestin, E. Moser, G. Sánchez, and L. Pavesi, *Sol. Energy Mater. Sol. Cells* **132**, 267 (2015).
33. G. Shao, C. Lou, and D. Xiao, *J. Lumin.* **157**, 344 (2015).
34. M. C. Beard, K. P. Knutsen, P. Yu, J. M. Luther, Q. Song, W. K. Metzger, R. J. Ellingson, and A. J. Nozik, *Nano Lett.* **7**, 2506 (2007).
35. A. Gali, M. Vörös, D. Rocca, G. T. Zimanyi, and G. Galli, *Nano Lett.* **9**, 3780 (2009).
36. A. J. Nozik, M. C. Beard, J. M. Luther, M. Law, R. J. Ellingson, and J. C. Johnson, *Chem. Rev.* **110**, 6873 (2010).
37. O. E. Semonin, J. M. Luther, S. Choi, H.-Y. Chen, J. Gao, A. J. Nozik, and M. C. Beard, *Science* **334**, 1530 (2011).
38. A. Franceschetti and Y. Zhang, *Phys. Rev. Lett.* **100**, 136805 (2008).
39. E. Rabani and R. Baer, *Nano Lett.* **8**, 4488 (2008).
40. S. Guha and J. Yang, NREL, 2005.
41. S. Guha and J. Yang, *IEEE Trans. Electron Devices* **46**, 2080 (1999).
42. J. Meier, R. Flückiger, H. Keppner, and A. Shah, *Appl. Phys. Lett.* **65**, 860 (1994).
43. L. T. Canham, *Appl. Phys. Lett.* **57**, 1046 (1990).
44. C. Delerue, G. Allan, and M. Lannoo, *Phys. Rev. B* **48**, 11024 (1993).
45. Y. Kanemitsu, *Phys. Rev. B*, **53**, 13515 (1996).
46. F. Gourbilleau, C. Ternon, D. Maestre, O. Palais, and C. Dufour, *J. Appl. Phys.* **106**, 013501 (2009).
47. D. Maestre, O. Palais, D. Barakel, M. Pasquinelli, C. Alfonso, F. Gourbilleau, M. D. Laurentis, and A. Irace, *J. Appl. Phys.* **107**, 064321 (2010).
48. B. Rezgui, A. Sibai, T. Nychporuk, M. Lemiti, and G. Brémond, *J. Vac. Sci. Technol. B* **27**, 2238 (2009).
49. E.-C. Cho, S. Park, X. Hao, D. Song, G. Conibeer, S.-C. Park, and M. A. Green, *Nanotechnology* **19**, 245201 (2008).
50. F. Gourbilleau, X. Portier, C. Ternon, P. Voivenel, R. Madelon, and R. Rizk, *Appl. Phys. Lett.* **78**, 3058 (2001).

51. G. Conibeer, *Mater., Today* **10**, 42 (2007).
52. C. Ternon, C. Dufour, F. Gourbilleau, and R. Rizk, *Eur. Phys. J. B - Condens. Matter Complex Syst.* **41**, 325 (2004).
53. A. R. Forouhi and I. Bloomer, *Phys. Rev. B* **34**, 7018 (1986).
54. C. Ternon, F. Gourbilleau, X. Portier, P. Voivenel, and C. Dufour, *Thin Solid Films* **419**, 5 (2002).
55. M. Roussel, E. Talbot, C. Pareige, R. P. Nalini, F. Gourbilleau, and P. Pareige, *Appl. Phys. Lett.* **103**, 203109 (2013).
56. A. Achiq, R. Rizk, F. Gourbilleau, and P. Voivenel, *Thin Solid Films* **348**, 74 (1999).
57. M. Roussel, E. Talbot, P. Pareige, and F. Gourbilleau, *J. Appl. Phys.* **113**, 063519 (2013).
58. O. Debieu, R. P. Nalini, J. Cardin, X. Portier, J. Perrière, and F. Gourbilleau, *Nanoscale Res. Lett.* **8**, 31 (2013).
59. V. A. Volodin, T. T. Korchagina, J. Koch, and B. N. Chichkov, *Phys. E Low-Dimens. Syst. Nanostructures* **42**, 1820 (2010).
60. Y. C. Peng, G. S. Fu, W. Yu, S. Q. Li, and Y. L. Wang, *Semicond. Sci. Technol.* **19**, 759 (2004).
61. Y. Lambert, D. Zhou, T. Xu, O. Cristini, D. Deresmes, B. Grandidier, and D. Stiévenard, *Appl. Phys. Lett.* **103**, 051102 (2013).
62. D. Zhou, Y. Pennec, B. Djafari-Rouhani, O. Cristini-Robbe, T. Xu, Y. Lambert, Y. Deblock, M. Faucher, and D. Stiévenard, *J. Appl. Phys.* **115**, 134304 (2014).